PAPER

X-ray induced modifications in U87 glioma cells probed by Raman- and infrared-based spectromicroscopy†

T. Senapati, [ID] [a] M. R. Bittermann, [ID] [a] R. Nadar,[b] A. van der Meer,[b] B. Kästner, [ID] [c] A. G. Denkova [ID] [b] and E. Rühl [ID] *[a]

A combination of spontaneous Raman, stimulated Raman, and photothermal expansion (AFM-IR) spectromicroscopy is reported for probing the impact of different radiation doses (2–10 Gy) on U87 glioma cells *ex vivo*. Most significant are alterations in spectral profiles caused by radiation-induced changes, while keeping the cell fixation delay constant at 24 h. The changes in delay of the fixation ranging up to 5 d at a dose of 2 Gy were also investigated for probing cellular recovery processes of exposed cells. Both, the Raman-based and AFM-IR spectral analyses identified statistically significant spectral changes and radiation-induced alterations in cellular proteins, nucleic acids, and lipids. Specifically, these label-free approaches revealed a 3-fold and 2-fold decrease in nucleic acid and lipid content, respectively, for cells treated with 10 Gy compared to untreated control samples. This study unravels the potential of a combination of Raman-based approaches and AFM-IR that is of use for therapeutics and offers a novel way to monitor and localize radiotherapy-induced changes in tumor cells.

1. Introduction

Gliomas consist of a group of central nervous system (CNS) tumors with characteristics of neuroglial cells, such as astrocytes and oligodendrocytes with an incidence rate of 3.19 per 100 000 population.[1] Specifically, glioblastoma defined as isocitrate dehydrogenase 1 or 2 (IDH) wildtype is the most malignant and aggressive type of glioma according to the World Health Organization (WHO) and the median survival time post-diagnosis is only 10–15 months, with a five-year survival rate of approximately 5%.[2,3] In this context, radiotherapy and temozolomide (TMZ) chemotherapy are the most widely used treatment strategies owing to their effectiveness in reducing tumor size, progression, alleviating symptoms, and enhancing the patient's quality of life.[4] Nearly 50% of all cancer patients undergo radiotherapy at some stage of their treatment,[5] highlighting the importance of research in the field. There exist different techniques including diffusion tensor imaging (DTI), diffusion-weighted imaging (DWI), magnetic resonance spectroscopy (MRS) and perfusion-weighted imaging (PWI) for imaging and mapping of post-treatment changes in gliomas.[6] However, these techniques lack chemical specificity needed to understand X-ray-induced cellular changes on the molecular level following radiotherapy that would be beneficial for optimizing treatment strategies.

Biological matter has been successfully probed by a variety of different spectromicroscopy techniques.[7] Often used were fluorescence labels, as these provide sensitive detection reaching even the single molecule detection limit.[8] Spatial resolution can significantly exceed the diffraction limit of optical microscopy, if such super-resolution techniques are employed.[9] However, this limits the probing to fluorescent species, which does not include biological species of interest that might be of importance to be probed following radiotherapy. Therefore, label-free spectromicroscopy is an elegant and sensitive approach for probing the species of interest by vibrational or electronic transitions at high spatial resolution.[7] Specific techniques of label-free spectromicroscopy include, *e.g.*, Raman-based techniques,[10–12] photothermal expansion,[13,14] and X-ray absorption.[15–17]

Modern spectroscopic techniques, such as spontaneous Raman spectroscopy, stimulated Raman spectroscopy (SRS), and atomic force microscopy-based infrared spectroscopy relying on photothermal expansion (AFM-IR) are powerful approaches for analyzing biological matter on the molecular-level as well as for observing therapeutically induced

[a] Freie Universität Berlin, Physikalische Chemie, Institut für Chemie und Biochemie, Arnimallee 22, 14195 Berlin, Germany. E-mail: ruehl@zedat.fu-berlin.de
[b] Radiation Science and Technology, Delft University of Technology, Mekelweg 15, 2629 JB Delft, The Netherlands
[c] Physikalisch-Technische Bundesanstalt (PTB), Abbestr. 2-12, 10587 Berlin, Germany

changes.[18–20] Raman spectroscopy, in particular, enables the identification of proteins, lipids, and nucleic acids without adding any labels. SRS enhances sensitivity, enabling rapid, spectral mapping of cellular components with an improved signal-to-noise ratio compared to spontaneous Raman scattering. AFM-IR, in contrast, directly measures infrared absorption at the nanoscale by photothermal expansion, overcoming the diffraction-limited resolution of conventional IR spectroscopy.[13] Additionally, AFM-IR provides information on complementary mechanical properties of the sample, which may also reflect radiation-induced cellular damage. Regarding studies based on Raman and infrared spectromicroscopy, *e.g.*, Qiu *et al.* developed a laser tweezer Raman spectroscopy technique to detect radiation therapy-induced changes in nasopharyngeal carcinoma cells.[21] Similarly, earlier work focused on developing an infrared microspectroscopy-based strategy for monitoring nanoparticle radiotherapy-treated F98 and U87-MG glioma cells.[22] Raman-based techniques were also used to study the classification and progression of other types of cancers, *e.g.* affecting skin, bladder or breast,[18,23] and to probe complex processes, such as cell cycle variations in brain cancer cells by combining Raman data acquisition with principal component-based data analysis.[24] AFM-IR was used to study the effect of different types of radiation on gliablastoma cells[25] and how X-rays induce biological responses in prostate cancer cells.[26] However, a comprehensive multimodal approach integrating Raman-based- and AFM-IR-based spectromicroscopy for probing spatially and spectrally resolved X-ray-induced molecular and structural changes of sub-cellular compartments in glioma cells remains largely unexplored.

In this work, we report on an experimental and data-analysis based approach using a combination of AFM-IR as well as spontaneous and stimulated Raman spectromicroscopy,[26] for detecting radiation-induced changes in U87 brain tumor cells. These cells were exposed to different doses of X-rays ranging from 2 Gy to 10 Gy. Furthermore, variations in delay times of cell fixation after exposure are reported ranging from immediate fixation (0 d) to 5 d. Specific spectral signature changes in exposed cells in comparison to control cells are probed. Furthermore, we gained from label-free spectromicroscopy approaches insights on X-ray-induced changes in tumor cells on a molecular level that are promising for determining the mechanisms of radiotherapy and their impact on a cellular level.

2. Experimental

2.1 Cell cultures

U87 tumor cells (Delft, The Netherlands) were thawed from a frozen stock (−196 °C) and seeded in a cell culture medium containing high glucose (4.5 g L^{-1}) Dulbecco's modified Eagle's medium (DMEM), supplemented with 10% fetal bovine serum (South American origin) and 1% combined 6 mg L^{-1} penicillin and 10 mg L^{-1} streptomycin antibiotics (Biowest). The cells were subcultured every 5 to 7 d (at approximately 80% cell confluency), using 1 mL (Biowest) trypsin to resuspend the cells. The concen-

tration of cells per mL was determined using an automated Luna2 cell counter (Westburg). Cells were kept in a humidified incubator at 37 °C and 5% CO_2. U87 cells were then seeded on a 2D surface. The cell density was adjusted on different substrates to match the experimental requirements. 1 mL cell culture was used to cover the area of each Kevley slide with approximately 90% in a 9 cm Petri dish (100 000 cells per mL) for Raman spectromicroscopy measurements and 30 μL containing 3000 cells was used to cover *ca.* 90% of each silicon wafer/Si substrate in a 6-well culture plate (100 000 cells per mL) for AFM-IR measurements. The cells were allowed to grow for 48 h until a monolayer of cells was clearly visible by optical microscopy.

2.2 Treatment of U87 tumor cells by X-rays

A XYLON X-ray tube with a tungsten anode was used for the radiation treatment to generate X-rays (Xylon International GmbH, Y.TU 320-D03 equipped with a 3 mm Be-filter). The instrument setup was as follows: 312 kV, 5 mA, a 4 mm Cu-filter was used to harden the X-ray beam, and the distance from the radiation source to the samples was 30 cm. Samples from groups 2, 3, and 4 were exposed to radiation doses of 2 Gy, 6 Gy, and 10 Gy in 10 min, respectively. The entire area of slides and wafers was irradiated with X-rays. After X-ray exposure, control (group 1) and the other samples were placed in an incubator at 37 °C for 24 h post-incubation. The samples were subsequently gently washed twice with PBS before proceeding with the fixation and staining protocols. After fixation, the cells were washed again gently and slowly with PBS. 4% *para*-formaldehyde was slowly added to the glass slide or silicon wafer until the whole section of cells was immersed in 4% PFA for 10 min. Post-fixation of the samples was accomplished by drying in open air and then they were sealed in a Falcon tube. NucBlue™ Live ReadyProbes™ reagent was used to stain the cell nuclei of the fixed samples by adding some drops of the reagent and leaving the samples for 10 min at ambient conditions. The above treatment group was further subdivided into stained and not stained ones to determine the influence of staining on the spectroscopic measurements.

2.3 Sample preparation for spectromicroscopy studies

The cells were prepared using two different protocols. In the first set of samples, U87 cells were exposed to doses ranging between 0 Gy and 10 Gy and were fixed after an incubation period, corresponding to a fixation delay, of 24 h. The second set of samples involved cells exposed to a 2 Gy dose, while varying the delays of fixation, ranging from immediate fixation after irradiation (0 d), 1 day (1 d), up to five days (5 d). For the Raman-based studies 10 cells were investigated for each dose. For the fixation delay studies 5 cells per time point were used. For the AFM-IR studies, 20 cells were measured for both dose-dependent and fixation delay studies.

2.4 AFM-IR spectromicroscopy

AFM-IR investigations of U87 cells employed a nano-IR2-s spectrometer (Anasys, Anaheim, CA, U.S.A./Bruker, Karlsruhe, Germany).[14,27] The AFM was equipped with a 450 μm long

gold-coated silicon AFM tip with a nominal radius of 500 nm (Nanotec, model: LRCH-500), operating at a resonance frequency of 15 ± 4 kHz and a spring constant of 0.2 N m^{-1}. Such large tip was chosen to enhance sensitivity and to facilitate experiments with full spectral coverage of entire cells within a reasonable data acquisition time. AFM-IR-spectra were collected at a sweep speed of 100 cm^{-1} per second and with a spectral step width of 1 cm^{-1}. The infrared laser power of the quantum cascade laser (MIRcat Daylight Solutions) applied to the sample was averaged of the order of ~1 mW. The repetition rate of the laser was adjusted automatically between 150 kHz and 220 kHz to match the contact resonance frequency of the cantilever. All spectra were background-corrected by the power spectrum of the laser. Spectral data were recorded with a spatial resolution of 1 μm in x- and y-directions, acquiring a full AFM-IR spectrum at each point. Considering the nominal tip radius of 500 nm, corresponding to a spatial resolution of ≈500 nm, this step size was chosen to balance reasonably fast data acquisition with an acceptable level of cell coverage. We have recently proposed a low-rank matrix reconstruction technique that would allow large cell coverage within reasonable acquisition time for which the AFM-IR instrument needs to be modified accordingly.[27] AFM-IR spectra were recorded from 1300 cm^{-1} to 1900 cm^{-1} for ~50 to 150 spectra per cell consisting of 20 cells per sample. All spectra were normalized to their minima and maxima and smoothed by a Savitzky–Golay filter order of 2 with a window length of 13. We note that compared to conventional FTIR, this approach delivers sub-micron-resolved infrared spectra from individual cells using a simple setup and reasonably short data acquisition times.

2.5 Raman-based spectromicroscopy

2.5.1 Spontaneous Raman spectromicroscopy. Raman spectra of U87 tumor cells were collected in the wavenumber range from 600 cm^{-1} to 1900 cm^{-1} using a modified optical microscope (BX41, Olympus) with a 100× objective lens (MPLN, Olympus).[12] A continuous-wave 532 nm laser (Millennia, 5 W, Spectra Physics) was used as a photon source and the scattered light was collected by fiber-optics that are coupled to a triple 80 cm spectrometer (Dilor XY 800, Horiba) equipped with a Peltier-cooled Synapse CCD detector (Horiba). To prevent thermal damage to the samples, the laser power was limited to approximately 5 mW. Raman spectra were recorded at each point within the selected region by taking two measurements per point and an integration time of 200 s at a spatial step size of 0.25 μm. The wavenumber resolution of the 1024-point Raman spectra was around 2.5 cm^{-1} using an entrance slit of 200 μm. Interferences from the glass slide beneath the biological samples were avoided by carefully adjusting the focus of the laser beam. To ensure the robustness of the results as well as to account for the natural variability of the exposed cells a ratiometric statistical analysis was performed, which covered 10 cells.[28]

2.5.2 Stimulated Raman spectromicroscopy. We employed stimulated Raman spectromicroscopy (SRS) for the experiments, with the experimental setup described previously.[12,29] Briefly, the samples were placed on an Olympus IX83 inverted microscope using a 100× near-infrared objective. The photon source was a PicoEmerald (APE) laser system, which emits on the same axis two correlated pulses: (i) a fixed-wavelength Stokes pulse at 1064.2 nm and (ii) a variable-wavelength pump pulse generated by an optical parametric oscillator.[12,29] SRS detection was achieved by measuring the stimulated Raman loss, with the Stokes beam modulated at 20 MHz using an electro-optical modulator. Modulations in the transmitted pump beam were captured by a fast photodiode and processed by a lock-in amplifier (Zurich Instruments). To prevent sample damage, the laser power was limited to 10 mW for the pump beam and 25 mW for the Stokes beam. Stimulated Raman maps were created by scanning the microscope stage (Merzhäuser, Wetzlar, Germany) with a dwell time of 160 ms per location. Background signals were taken at 1900 cm^{-1} (885.2 nm), where no Raman signal from tumor samples occurs.

The pump wavelength (λ_{pump}) was fine-tuned to match the energy difference between the pump- and Stokes-beams with the vibrational wavenumber ($\tilde{\nu}$) of interest, according to eqn (1):

$$\lambda_{\text{pump}} = \frac{1}{\dfrac{1}{1064\,\text{nm}} + 10^{-7}\,(\text{cm}\,\text{nm}^{-1}) \cdot \tilde{\nu}}, \qquad (1)$$

where $\tilde{\nu}$ is given in cm^{-1}. Biological components, such as nucleic acids, lipids, tyrosine/tryptophan, amide I and amide II vibrations were mapped at the following wavenumbers: 1097 cm^{-1}, 1730 cm^{-1}, 1615 cm^{-1}, 1662 cm^{-1}, and 1578 cm^{-1}, respectively. The background signal was mapped at 1900 cm^{-1} and subtracted from other maps. The dimensions of the maps were 25×25 μm for each cell. In all spectroscopic methods employed in this study we focused on the fingerprint region, including the spectral range encompassing the amide I and amide II peaks along with the CO stretching mode of lipids. This regime provides a compact overview of nucleic acids, proteins, lipids, and their modifications.

2.6 Data analysis

AFM-IR and spontaneous Raman spectra were evaluated using Python and Origin Lab. AFM-IR spectra were baseline corrected using a line, smoothed using a Savitzky–Golay filter (window length 13, polynomal order 2) and were subsequently normalized to their minima and maxima, respectively. A peak analysis between 1500 cm^{-1} and 1700 cm^{-1} was conducted by fitting Gaussians to the spectral regimes 1530 cm^{-1}–1560 cm^{-1}, 1630 cm^{-1}–1700 cm^{-1}, and 1710 cm^{-1}–1730 cm^{-1} for investigating amide II, amide I, and lipid bands, respectively. The area of each Gaussian was considered for the calculation of the peak ratios. Maps and optical images were processed by ImageJ and Origin Lab.

3. Results and discussion

3.1 AFM-IR spectral analysis on X-ray-exposed U87 cells

The workflow of the experiments is illustrated in Fig. 1A. The effect of irradiation by X-rays on U87 tumor cells was investi-
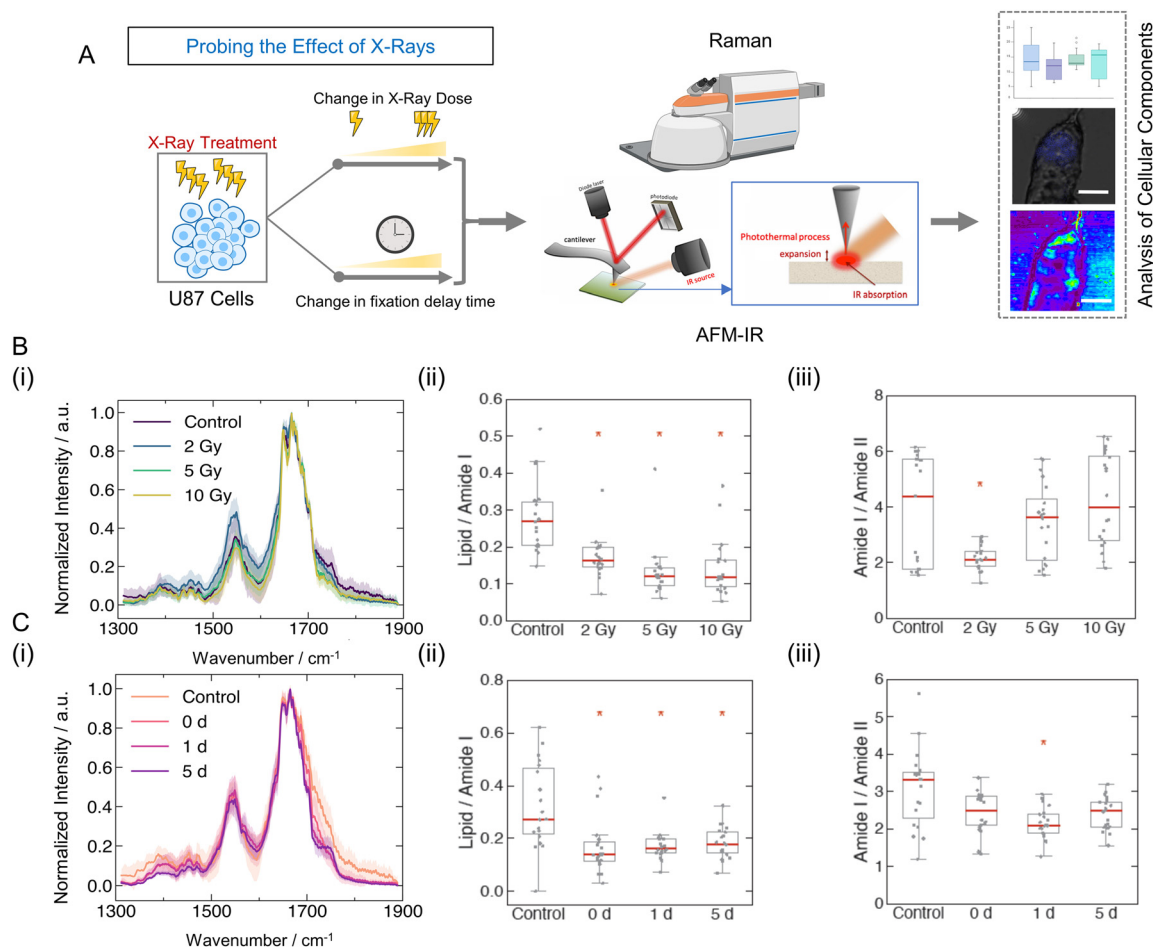
Fig. 1 (A) Schematic illustration of the experimental approach. The effect of the exposure of U87 cancer cells to X-rays is studied by a combination of label-free spectroscopic approaches (here: AFM-IR and Raman-based approaches). The average AFM-IR spectra for each sample are shown together with their standard deviations σ (shaded areas: $\pm\sigma$) as a function of dose in B(i) and as a function of delay in fixation in C(i) (see Fig. S2† for individual spectra). B(ii) and B(iii) show box whisker plots of the lipid-to-amide I-ratio ($1750\ cm^{-1}/1670\ cm^{-1}$) and the amide I-to-amide II-ratio ($1670\ cm^{-1}/1550\ cm^{-1}$) based on peak areas, respectively, measured in cells treated with radiation doses of 2 Gy, 5 Gy, and 10 Gy (fixed after 24 h). C(ii) and C(iii) show box whisker plots of the lipid-to-amide I-ratio ($1750\ cm^{-1}/1670\ cm^{-1}$) and the amide I-to-amide II-ratio ($1670\ cm^{-1}/1550\ cm^{-1}$) for cells exposed to a dose of 2 Gy cells and were fixed with different delays. Ratios were calculated from peak areas obtained from Gaussians deconvolutions (see section 2.6). The red stars indicate a significant difference obtained from a two-sample independent t-test ($p < 0.01$) between the means of the irradiated samples with respect to the unexposed control.

gated by photothermal expansion (AFM-IR), spontaneous Raman spectroscopy, and stimulated Raman spectroscopy (SRS) as label-free approaches. Samples exposed to different radiation doses and delays in fixation were analyzed for monitoring alterations in cellular markers and components, such as nucleic acids, lipids, and proteins that are spectroscopically identified.

First, we utilized AFM-IR to investigate spectral changes in X-ray-exposed U87 tumor cells compared to unexposed cells.[30] The cells were prepared using two different protocols, as described in section 2.1 and the spectral data were collected from entire cells (cf. Fig. S1†).[31] Averaged AFM-IR spectra of cells exposed to different radiation doses and fixation delays (see section 2.3) are presented in Fig. 1B(i) and C(i), respectively. The average AFM-IR spectra remain almost identical except for some vibrations within the weak C=O-stretching

band of lipids at $1750\ cm^{-1}$. A plot of the lipid-to-amide I-ratio[32] versus radiation dose was derived from the integrated peak areas of lipid and amide I bands. This intensity ratio decreases in irradiated cells due to a reduction in lipid intensity, with no apparent dose dependence (see Fig. 1B(ii)). This suggests possible disruptions of lipids within the cells upon irradiation with X-rays, which is rationalized by the fact that ionizing radiation can generate reactive oxygen radicals and H_2O_2 that are known to damage lipids and nucleic acids.[33] The amide I-to-amide II-ratio ($1670\ cm^{-1}/1550\ cm^{-1}$), does not show any significant changes for different X-ray doses (Fig. 1B(iii)). The 2 Gy sample appears lower, likely reflecting sample variability since the data were taken from the fixation-time dependent data series.

Further, the delay in fixation was varied while keeping the X-ray irradiation constant at 2 Gy to probe how the cellular

components evolve as a function of time. Previously, studies on the glycogen accumulation in tumor cells and its effect on fixation delay of post-irradiated cells were reported.[34] This revealed that the glycogen level is reduced immediately after treatment and subsequently recovered on day 3. In a similar context, to understand the effect of the cellular response over time in U87 cells, we investigated them at different fixation delays. When post-irradiation fixation delays were varied, the corresponding IR spectra (Fig. 1C(i)) reveal that the lipid-to-amide I-ratio clearly decreased for all fixation delays (Fig. 1C (ii)). This pattern suggests a significant impact of irradiation on the integrity of lipids already immediately after exposure. Variations in fixation delays lead to subtle changes that may contain indications for possible repair mechanisms. The amide I-to-amide II-ratio appears largely independent of irradiation and applied dose (Fig. 1C(iii)). This suggests a significant impact of radiation on the integrity of lipids immediately after exposure, followed by a possible cellular recovery starting around 1 d after irradiation. In contrast, the amide I-to-amide II-ratio remains almost unchanged for different fixation delays (Fig. 1C(iii)). These results indicate that AFM-IR monitors chemical changes in lipid components in U87 tumor cells by probing spectral changes that correlate both with the X-ray dose and fixation delay.

3.2 Spontaneous Raman spectral analysis of X-ray-exposed U87 cells

Spontaneous Raman spectroscopy was used to investigate spectral changes of the X-ray-treated cell populations and untreated reference samples. We used the same samples discussed in section 3.1, *i.e.*, probing U87 cells which were irradiated by X-ray doses of 2 Gy, 6 Gy, and 10 Gy, respectively, followed by a fixation delay of 24 h (1 d), and the samples in which a dose of 2 Gy was fixed but the fixation delay times varied. Spectral data of entire cells obtained from spontaneous Raman microscopy provide spatially resolved spectral information, as shown in Fig. S3† for each cell population. Average Raman spectra of these cells subjected to different radiation doses are shown in Fig. 2A(i) including standard deviations. Fig. S4A and S5A† show Raman spectra of single cells as well as the average of 10 cells. These results underscore the reproducibility of the results and evidence radiation-induced spectral changes. A dose-dependent variation in the lipid-to-amide I-ratio is observed, occurring at 1730 cm^{-1} and 1662 cm^{-1}, respectively. Evidently, the lipid intensity decreases with an increase in X-ray dose (Fig. 2A(ii)). The lipid intensity for 2 Gy-treated cells was reduced by ~20% with respect to the control cells, whereas 10 Gy-exposed cells show a ratio that is
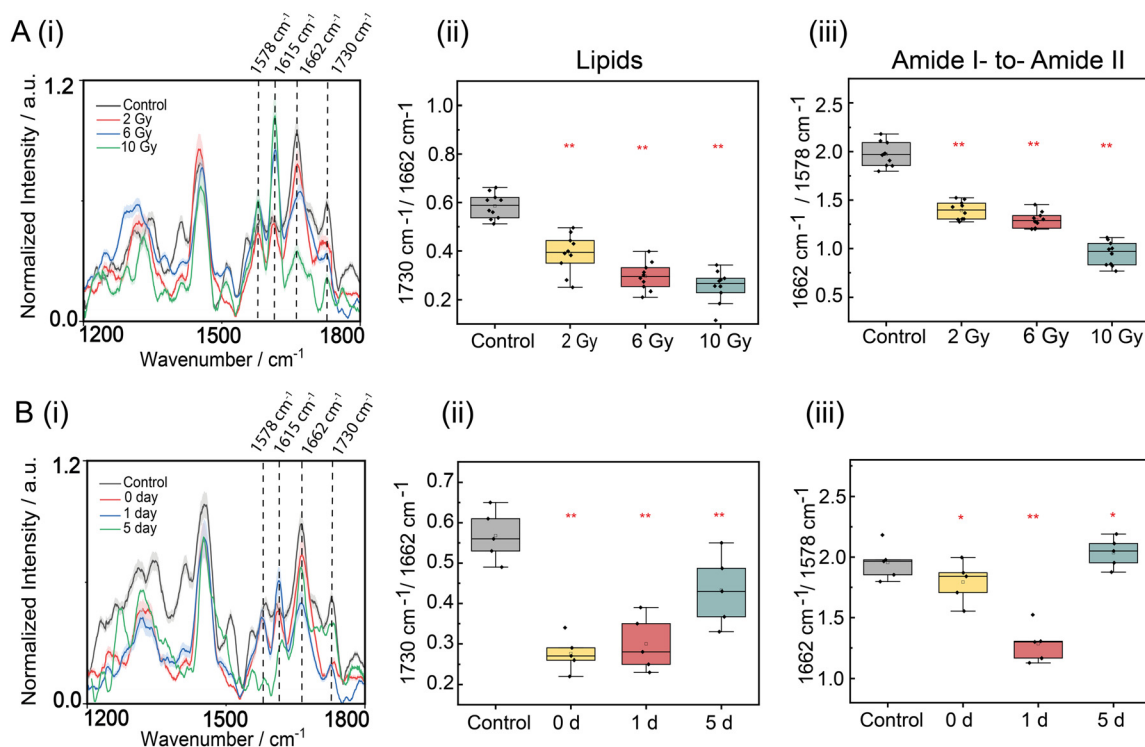

Fig. 2 Average Raman spectra (solid lines) with standard deviations σ (shaded areas: $\pm\sigma$) in the range of 1200–1800 cm^{-1}. A(i) Spectral changes of samples exposed to increasing radiation doses (2 Gy, 6 Gy, and 10 Gy) compared to an unexposed control sample; B(i) spectral changes at different fixation delays after initial 2 Gy irradiation (0, 1, and 5 days) compared to an unexposed control sample. Characteristic Raman peaks associated with molecular vibrations are indicated by vertical dashed lines at 1578, 1615, 1662, and 1730 cm^{-1}; A(ii) and B(ii) show the lipid-to-protein-ratio (1730 cm^{-1}/1662 cm^{-1}) obtained from A(i) and B(i), respectively; A(iii) and B(iii) show the amide I-to-amide II-ratio (1662 cm^{-1}/1578 cm^{-1}) obtained from A(i) and B(i), respectively. The *p*-value <0.05 is represented by (*) and *p* < 0.01 by (**).

decreased by ∼40%. This result indicates that there are changes in vibrations resulting from structural modifications within the ester carbonyl groups of diacylglycerol lipids as a result of X-ray exposure,[35] which is in agreement with the AFM-IR results (see Fig. 1B(ii)). Additionally, we observed significant spectral differences at 1662 cm^{-1} and 1578 cm^{-1}, the characteristic Raman bands of amide I and amide II, respectively. Examining the amide I-to-II-ratio (Fig. 2A(iii)) revealed a decrease in intensity with increasing X-ray doses. This indicates changes in protein secondary structure, which are due to alterations in C=O and C–N stretching vibrations in amide I (1662 cm^{-1}) followed by C–N and N–H vibrations in the amide II band. As a result, the amide I-to-amide II-intensity-ratio was reduced to 60% of that of the untreated cells if a dose of 2 Gy was applied. Higher doses of 6 and 10 Gy led to a larger decrease of this intensity ratio. This observation agrees with previous reports indicating that X-rays induce the formation of reactive oxygen species (ROS), causing damage to proteins, lipids, and nucleic acids, and possibly resulting in cell death.[33,36] This gradual increase in dose revealed detailed changes in cellular components due to varying levels of irradiation.[37] We note that the changes related to protein modifications are not observed in the AFM-IR data shown in Fig. 1B(iii) and C(iii), which underscores the need to employ different spectromicroscopy techniques.

The second set of experiments involved defined fixation delays ranging from immediately after exposure (0 d) to 5 d at a constant 2 Gy dose, as shown in Fig. 2B(i) including standard deviations. Fig. S4B† shows the data for all analyzed cells including average spectra. The lipid-to-amide I-ratio ($1730 \text{ cm}^{-1}/1662 \text{ cm}^{-1}$) initially decreased in the case of immediate fixation (0 d) and then gradually increased for longer fixation delays. This indicates immediate radiation damage followed by a gradual cellular recovery beginning after 1 d (see Fig. 2B(ii)) continuing to 5 d and agrees with the results obtained from AFM-IR measurements. The amide I-to-amide II-ratio ($1662 \text{ cm}^{-1}/1578 \text{ cm}^{-1}$) is reduced by up to ∼60% if the fixation is delayed by 1 d after exposure to a 2 Gy dose (Fig. 2B(iii)). Notably, after 5 d it is back to almost the same ratio as for unexposed control cells. This suggests substantial recovery of protein secondary structures between 1 d and 5 d after dose application. These observations demonstrate that lipid and protein structures in U87 tumor cells show immediate and progressive damage after exposure to high doses of X-rays. Fixation delay variations show cell recovery within days, offering valuable insights into the timeline of cellular repair mechanisms following radiation therapy. This technique was employed before to study breast cancer cells for early detection and diagnosis.[38]

Alongside the changes in the overall lipid and protein content, we also observed alterations in the nucleic acids profile in X-ray treated cell populations. Fig. 3A(i) illustrates the fingerprint Raman spectra showing the nucleic acids Raman-active band at 1097 cm^{-1} for samples exposed to varying X-ray doses. Fig. S5A† shows the data for all analyzed cells including average spectra. To highlight and quantify
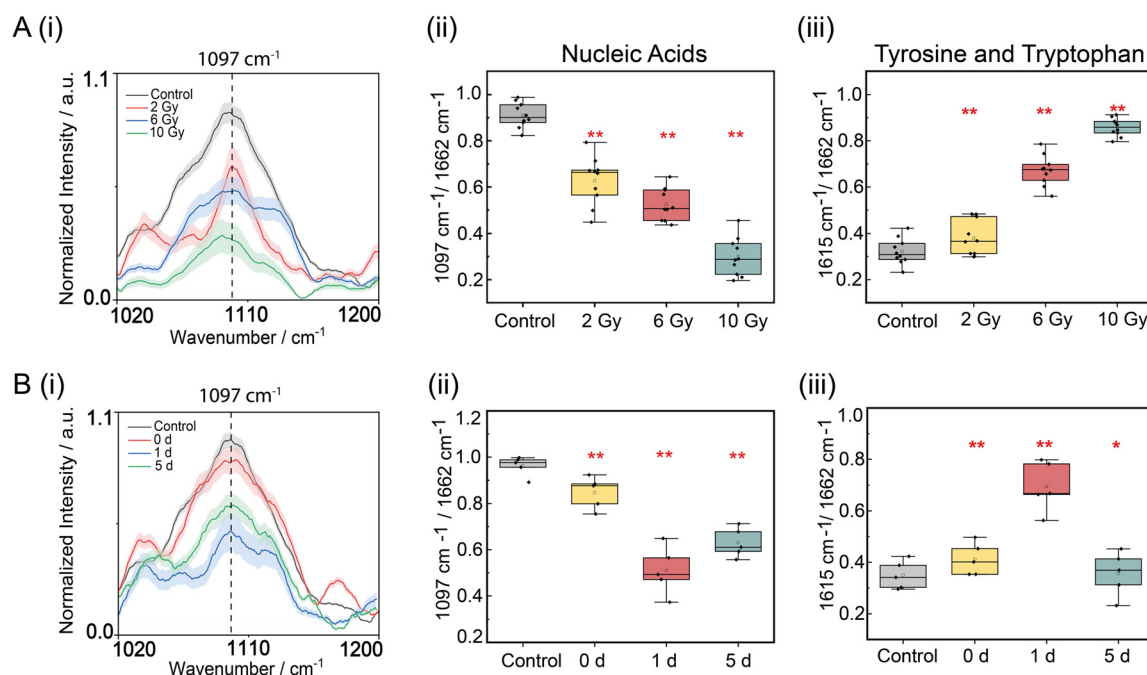

Fig. 3 Average Raman spectra (solid lines) with standard deviations σ (shaded areas: ±σ) in the range of $1020–1200 \text{ cm}^{-1}$ as a function of dose A(i) and fixation delay (B(i)) (cf. Fig. 1). A statistical analysis of the nucleic acid profile in response to the X-ray dose is shown in A(ii) and fixation delay B(ii). The p-value <0.05 is represented by (*) and p < 0.01 by (**). The Raman intensity comparison at $1615 \text{ cm}^{-1}/1662 \text{ cm}^{-1}$ (tyrosine and tryptophan) as a function of dose (A(iii)) and fixation delay (B(iii)) is also shown.

these spectral changes, a statistical analysis of the nucleic acids-to-amide I-ratio was performed. The box-whisker plot shown in Fig. 3A(ii) revealed a reduction in intensity of nucleic acids by factors of 1.5, 1.8, and 3 with increasing radiation doses of 2 Gy, 6 Gy, and 10 Gy, respectively. This observation can be attributed to both, radiation-induced bond cleavages and ROS-induced changes due to DNA/RNA strand breaks or cross-linking.[39,40]

Furthermore, significant changes of the Raman band around 1615 cm^{-1} are observed, which are primarily due to the amino acids tyrosine and tryptophan. The dose-dependent changes indicate an increase in intensity ratio from 10% to 60% as the dose is increased from 2 Gy to 10 Gy (Fig. 3A(iii)). The C=C stretching in tyrosine and tryptophan is affected by X-rays, demonstrating that the relative content of these amino acids probed by the ratio of Raman bands at 1615 cm^{-1}/ 1662 cm^{-1} was different in the case of irradiated cells compared to control cells, similar to earlier results reported by Qiu *et al.*[21]

For the second set of samples, where the fixation delay was varied while keeping the dose constant at 2 Gy, a decrease in intensity in the Raman spectrum around the 1097 cm^{-1} is observed, which is associated with the phosphate backbone of nucleic acids, as the fixation delay is increased (Fig. 3B(i), see also Fig. S5B†) for individual spectra of different cells. To strengthen this finding, a ratiometric statistical analysis of the nucleic acid-to-amide I-ratio was performed on multiple cells indicating a reduction in intensity by a factor of ~2 for fixation delays up to 1 d, and there is a ~15% increase after a delay of 5 d (Fig. 3B(ii)). This indicates cellular recovery with increasing fixation delays. For the time-dependent tyrosine- and trypto-phan-to-amide I-ratios we identified an increasing trend for up to 1 d fixation delay, followed by a complete recovery to the level of control cells (Fig. 3B(iii)). This reflects the dynamic response of tumor cells to radiation doses, with early damage to nucleic acids and amino acids, followed by indications of subsequent repair and recovery.

3.3 Stimulated Raman mapping analysis on U87 cells

Stimulated Raman scattering (SRS) mapping is used as a complementary approach to spontaneous Raman scattering by employing its strength in spatially resolved mapping of Raman bands with increased sensitivity.[11] SRS maps of individual cells were taken by using wavenumber specific maps of the key cellular components. For this, we focused on the sample set exposed to varying X-ray doses to investigate radiation-induced alterations in chemical composition. Optical micrographs of these samples are presented in Fig. 4A(i)–D(i), where the nucleus was stained by NucBlue. SRS microscopy was used to examine the spatial distribution of nucleic acids at 1097 cm^{-1} (Fig. 4A(ii)–D(ii)). In the unexposed control cells the intensity of nucleic acids near the nuclear region is higher with respect to the X-ray treated samples, indicating intact structures of nucleic acids. Reduced intensity in this spectral region indicates damage to nucleic acids, which is mostly due to the phosphate bonds of DNA.[21,41] The alteration in this stretching

vibration may also lead to a partial loss of the B-form geometry of DNA inside the tumor cell population followed by DNA fragmentation.[42]

Lipids are probed at 1730 cm^{-1} (Fig. 4A(iii)–D(iii)). These show well-defined patterns which likely correspond to the cell membranes and organelles. The X-ray-exposed cells exhibit a noticeable reduction in lipid intensity within the cells, indicating a degradation of lipid structures and lipid peroxidation, which are commonly associated with oxidative stress as a result of irradiation by X-rays.[43] These results agree with the spontaneous Raman and AFM-IR data, see Fig. S6–S9,† where other data sets revealing similar results are shown. Note that the enhanced signal strength outside the cells is not due to the bare substrate, rather this signal corresponds to intercellular regions, which are rich in extracellular vesicles, secreted lipids, or membrane debris. In addition, the amino acids, such as tyrosine and tryptophan, were probed at 1615 cm^{-1}, see Fig. 4A(iv)–D(iv). The overall intensity of these amino acids shows a homogeneous distribution in the entire cell regions for control cells, whereas X-ray exposed cells show a hetero-geneous pattern with increased intensity in some areas and depletion in others. This indicates structural protein modifications and aggregation due to the dose-dependent impact of X-rays. Finally, we examined the amide I-to-amide II-ratio (Fig. 4A(v)–D(v)) revealing a decrease with irradiation dose that agrees with the data obtained from spontaneous Raman spectromicroscopy. This suggests protein misfolding or degradation, which is an indication for cellular stress responses to X-rays.[44]

Cell heterogeneity needs to be considered, as cells may be probed in different states of the cell cycle. Therefore, we performed a statistical ratiometric analysis involving multiple cells for each sample, as shown in Fig. 4E(i)–(iv). This includes specific changes in nucleic acid, lipids, tyrosine and trypto-phan, as well as the amide I-to-amide II-ratio and complements single cell SRS maps. For example, the reduction of nucleic acids in cells treated with doses between 2 Gy and 10 Gy is indicated by increasingly blue-colored maps (see Fig. 4B (ii)–D(ii)) that are evaluated in greater detail in Fig. 4E(i). Specifically, a ~60% reduction in Raman signal that is due to nucleic acids is observed. Also, the lipid intensity shows a similar decrease as a function of dose, which is in accordance with the spontaneous Raman spectra discussed above.

Next, we analyzed the SRS maps for single cells in more detail, by focusing on the cellular regions where the nucleus is located, as indicated by staining. Since the nucleus is the main region of radiation-induced DNA damage, which is crucial for cell viability, apoptosis, and the response to cancer therapy, it is of special interest when investigating X-ray-induced alterations by stimulated Raman mapping.[26] Here, X-ray dose-dependent modifications in the nucleus were investigated by Raman mapping, rather than single-point measurements from this region, which provides a limited view on the overall dose response of cells. For each molecular component, *cf.* Fig. 4, we extracted the intensity values of each pixel within the nucleus regions and represented them as ridgeline plots demonstrating
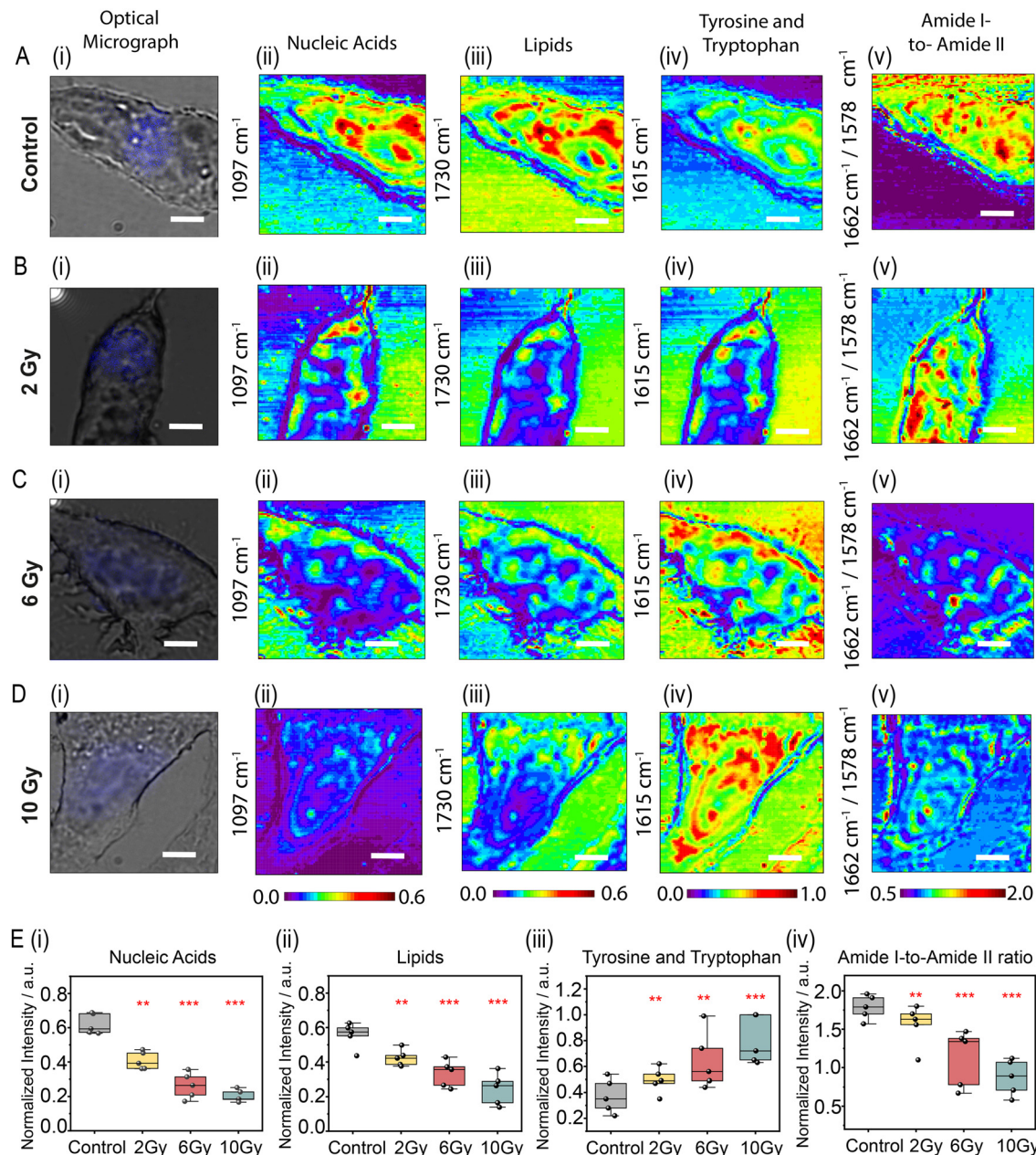
Fig. 4 Optical micrographs of the analyzed tumor cells. The A(i) control cell and cells treated with doses of B(i) 2 Gy, C(i) 6 Gy, and D(i) 10 Gy, respectively, are shown. The nuclei stained by NucBlue are visualized by optical microscopy. A(ii)−D(ii) corresponds to normalized SRS maps of nucleic acids recorded at 1097 cm^{-1}. A(iii)−D(iii) show normalized SRS maps of the lipid distribution of a control cell and cells exposed to 2 Gy, 6 Gy, and 10 Gy, respectively. A(iv)−D(iv) show normalized SRS maps of tyrosine and tryptophan. A(v)−D(v) show normalized maps of the amide I-to-amide II-ratio (1662 cm^{-1}/1578 cm^{-1}). E(i)−(iv) show statistical analyses of changes in (i) nucleic acids, (ii) lipids, (iii) the tyrosine-to-tryptophan-ratio, and (iv) the amide I-to-amide II-ratio for entire cells exposed to different X-ray doses. The box plots highlight significant intensity changes in the case of cellular components [p-value <0.05 (*), $p < 0.01$ (**), and $p < 0.001$ (***)]. Scale bars: 5 μm.

key features within this cellular compartment (Fig. 5A–D). For nucleic acids (Fig. 5A), X-ray irradiated samples showed curve shifts towards lower intensity, suggesting DNA fragmentation or chromatin relaxation.[45] Fig. 5B shows well-defined lipid intensity for the control sample, whereas events associated with lower lipid intensity become more frequent with increasing X-ray dose highlighting lipid degradation and oxidative damage. Tyrosine

and tryptophan intensity also shows a shift in mean intensity reflecting structural alterations in nuclear proteins (Fig. 5C). The amide I-to-amide II-ratio (Fig. 5D) highlights that control cells exhibit a higher frequency of events having intensity greater than the mean intensity, whereas X-ray treated samples show a shift towards lower intensity implying unfolding or conformational rearrangements in nuclear proteins.
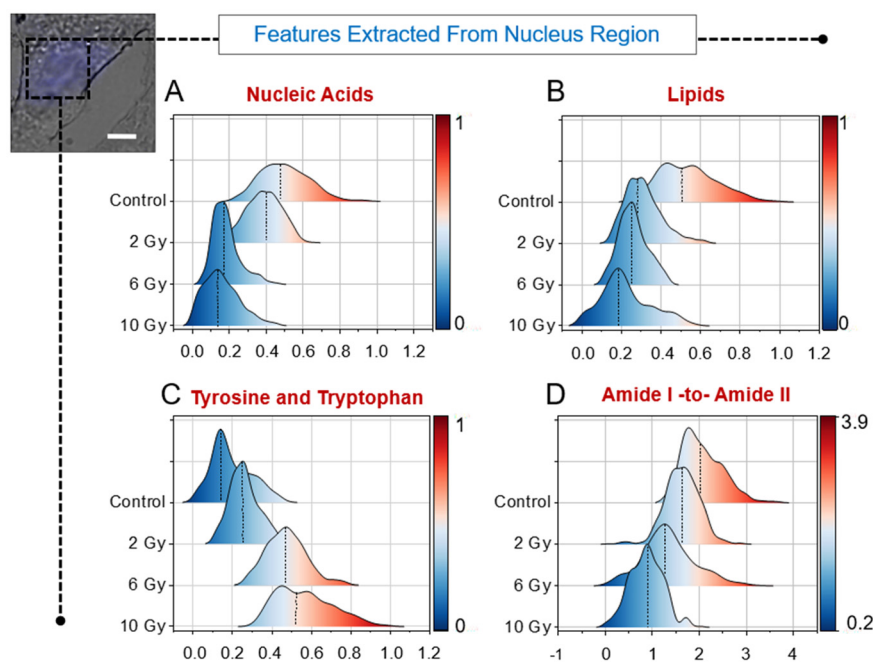
Fig. 5 Features extracted from the nucleus region of U87 cells at different X-ray doses. The top-left micrograph shows the highlighted nucleus region (scale bar: 5 μm). Statistical analysis of SRS maps for cellular components including A nucleic acids, B lipids, C tyrosine and tryptophan, and D the amide I-to-amide II-ratio. The abscissa represents intensity and the ordinate represents frequency. The distributions reveal dose-dependent changes in molecular profiles, with normalized intensity scales shown for each spectral feature. The average of each distribution is shown by the dotted vertical lines. The distribution of the relative intensity variation is reflected by the color bar.

Notably, the observed changes in the nucleus closely mirror those observed in the entire cells by SRS maps (Fig. 4E(i)–(iv)), further indicating the consistency of radiation-induced changes in different cellular regions. Significant shifts in the distribution of all components (nucleic acids, lipids, and proteins) within the region of the nucleus occur at any dose, with the most significant changes occurring when exposing the cells to the highest dose of 10 Gy. We note that further investigations are required to detail micro-structural changes for specific cancer/tumor cell types in greater detail.

lipids was observed with increasing dose. Raman spectra could retrieve the fine heterogeneity of the samples, while AFM-IR provides details on the local chemical composition of cells. Stimulated Raman maps of single cells provide spatial distributions and dose-dependent changes of proteins, lipids, and nucleic acids. The region of the cell nucleus was studied in detail providing a comprehensive view of the response to X-ray doses of this sub-cellular compartment. The results from this research can be useful for an improved understanding of radiation therapy for treating tumor diseases.

4. Conclusions

In summary, U87 cells were exposed to X-rays and dose-dependent changes were investigated by label-free spectromicroscopy including AFM-IR, spontaneous Raman spectroscopy, and stimulated Raman scattering. These techniques yield largely consistent results and complement each other, providing insights into radiation-induced chemical changes deduced from spectroscopic patterns by label-free spectromicroscopy. The tumor cells were studied by varying the X-ray doses (2 Gy, 6 Gy, and 10 Gy), and fixation delays of 0 d, 1 d, and 5 d after irradiation with 2 Gy. The sensitivity of these techniques for the detection of subtle spectroscopic changes within the cells allowed us to evaluate changes in proteins, lipids, and nucleic acids as a function of dose and repair mechanisms probed by delayed fixation. Specifically, a decrease in nucleic acids and

Author contributions

T. S.: conduction of AFM-IR- and Raman-based spectromicroscopy studies, data evaluation, writing the first draft of the manuscript. M. R. B.: conduction of AFM-IR studies, AFM-IR data evaluation, and editing the manuscript. R. N.: growing of cells, irradiation of cells, editing the manuscript. A. M.: growing of cells, irradiation of cells, editing the manuscript. B. K.: design of the scientific problem, editing the manuscript. A. G. D.: design of the scientific problem, writing, and editing the manuscript. E. R.: design of the scientific problem, writing, and editing the manuscript.

Conflicts of interest

The authors declare no conflict of interest.

Data availability

Additional datasets supporting this work have been included as part of the ESI.†

The datasets generated and analyzed during this work can be made available from the authors on request.

Acknowledgements

References

1 A. F. Tamimi and M. Juweid, in *Glioblastoma*, ed. S. De Vleeschouwer, Codon Publications, Brisbane (AU), 2017.

2 D. N. Louis, A. Perry, P. Wesseling, D. J. Brat, I. A. Cree, D. Figarella-Branger, C. Hawkins, H. K. Ng, S. M. Pfister, G. Reifenberger, R. Soffietti, A. von Deimling and D. W. Ellison, *Neuro-Oncology*, 2021, **23**, 1231–1251.

3 Q. T. Ostrom, G. Cioffi, K. Waite, C. Kruchko and J. S. Barnholtz-Sloan, *Neuro-Oncology*, 2021, **23**, iii1–iii105.

4 M. Koshy, J. L. Villano, T. A. Dolecek, A. Howard, U. Mahmood, S. J. Chmura, R. R. Weichselbaum and B. J. McCarthy, *J. Neuro-Oncol.*, 2012, **107**, 207–212.

5 G. Delaney, S. Jacob, C. Featherstone and M. Barton, *Cancer*, 2005, **104**, 1129–1137.

6 R. Stupp, W. P. Mason, M. J. van den Bent, M. Weller, B. Fisher, M. J. B. Taphoorn, K. Belanger, A. A. Brandes, C. Marosi, U. Bogdahn, J. Curschmann, R. C. Janzer, S. K. Ludwin, T. Gorlia, A. Allgeier, D. Lacombe, J. G. Cairncross, E. Eisenhauer, R. O. Mirimanoff, D. Van Den Weyngaert, S. Kaendler, P. Krauseneck, N. Vinolas, S. Villa, R. E. Wurm, M. H. B. Maillot, F. Spagnolli, G. Kantor, J. P. Malhaire, L. Renard, O. De Witte, L. Scandolaro, C. J. Vecht, P. Maingon, J. Lutterbach, A. Kobierska, M. Bolla, R. Souchon, C. Mitine, T. Tzuk-Shina, A. Kuten, G. Haferkamp, J. de Greve, F. Priou, J. Menten, I. Rutten, P. Clavere, A. Malmstrom, B. Jancar, E. Newlands, K. Pigott, A. Twijnstra, O. Chinot, M. Reni, A. Boiardi, M. Fabbro, M. Campone, J. Bozzino, M. Frenay, J. Gijtenbeek, A. A. Brandes, J. Y. Delattre, U. Bogdahn, U. De Paula, M. J. van den Bent, C. Hanzen, G. Pavanato, S. Schraub, R. Pfeffer, R. Soffietti, M. Weller, R. D. Kortmann, M. Taphoorn, J. L. Torrecilla, C. Marosi, W. Grisold, P. Huget, P. Forsyth, D. Fulton, S. Kirby, R. Wong, D. Fenton, B. Fisher, G. Cairncross, P. Whitlock, K. Belanger, S. Burdette-Radoux, S. Gertler, S. Saunders, K. Laing, J. Siddiqui, L. A. Martin, S. Gulavita, J. Perry, W. Mason, B. Thiessen, H. Pai, Z. Y. Alam, D. Eisenstat, W. Mingrone, S. Hofer, G. Pesce, J. Curschmann, P. Y. Dietrich, R. Stupp, R. O. Mirimanoff, P. Thum, B. Baumert and G. Ryan, *N. Engl. J. Med.*, 2005, **352**, 987–996.

7 U. Alexiev and E. Rühl, in *Drug Delivery and Targeting*, ed. M. Schaefer-Korting and U. Schubert, Springer Nature Switzerland, Cham, 2023, pp. 153–189.

8 P. Volz, A. Boreham, A. Wolf, T.-Y. Kim, J. Balke, J. Frombach, S. Hadam, Z. Afraz, F. Rancan, U. Blume-Peytavi, A. Vogt and U. Alexiev, *Int. J. Mol. Sci.*, 2015, **16**, 6960–6977.

9 K. Prakash, B. Diederich, R. Heintzmann and L. Schermelleh, *Philos. Trans. R. Soc., A*, 2022, **380**, 20210110.

10 G. J. Zhang, D. J. Moore, C. R. Flach and R. Mendelsohn, *Anal. Bioanal. Chem.*, 2007, **387**, 1591–1599.

11 C. W. Freudiger, W. Min, B. G. Saar, S. Lu, G. R. Holtom, C. W. He, J. C. Tsai, J. X. Kang and X. S. Xie, *Science*, 2008, **322**, 1857–1861.

12 A. Klossek, S. Thierbach, F. Rancan, A. Vogt, U. Blume-Peytavi and E. Rühl, *Eur. J. Pharm. Biopharm.*, 2017, **116**, 76–84.

13 A. Dazzi and C. B. Prater, *Chem. Rev.*, 2017, **117**, 5146–5173.

14 G. Germer, L. Schwartze, J. García-Miller, R. Balansin-Rigon, L. J. Groth, I. Rühl, P. Patoka, C. Zoschke and E. Rühl, *Analyst*, 2024, **149**, 2122–2130.

15 K. Yamamoto, R. Flesch, T. Ohigashi, S. Hedtrich, A. Klossek, P. Patoka, G. Ulrich, S. Ahlberg, F. Rancan, A. Vogt, U. Blume-Peytavi, P. Schrade, S. Bachmann, M. Schäfer-Korting, N. Kosugi and E. Rühl, *Anal. Chem.*, 2015, **87**, 6173–6179.

16 K. Yamamoto, A. Klossek, R. Flesch, T. Ohigashi, E. Fleige, F. Rancan, J. Frombach, A. Vogt, U. Blume-Peytavi, P. Schrade, S. Bachmann, R. Haag, S. Hedtrich, M. Schäfer-Korting, N. Kosugi and E. Rühl, *J. Controlled Release*, 2016, **242**, 64–70.

17 G. Germer, T. Ohigashi, H. Yuzawa, N. Kosugi, R. Flesch, F. Rancan, A. Vogt and E. Rühl, *ACS Omega*, 2021, **6**, 12213–12222.

18 J. B. Xu, T. Yu, C. E. Zois, J. X. Cheng, Y. G. Tang, A. L. Harris and W. E. Huang, *Cancers*, 2021, **13**, 1718.

19 S. S. Cui, S. Zhang and S. H. Yue, *J. Healthcare Eng.*, 2018, **2018**, 8619342.

20 A. dos Santos, N. Hondl, V. Ramos-Garcia, J. Kuligowski, B. Lendl and G. Ramer, *ACS Meas. Sci. Au*, 2023, **3**, 301–314.

21 S. F. Qiu, Y. L. Weng, Y. Li, Y. Chen, Y. H. Pan, J. Liu, W. Z. Lin, X. C. Chen, M. M. Li, T. Lin, W. Liu, L. R. Zhang and D. Lin, *RSC Adv.*, 2020, **10**, 14368–14373.

22 I. Martinez-Rovira, O. Seksek and I. Yousef, *Analyst*, 2019, **144**, 6352–6364.

23 S. Devpura, K. N. Barton, S. L. Brown, O. Palyvoda, S. Kalkanis, V. M. Naik, F. Siddiqui, R. Naik and I. J. Chetty, *Med. Phys.*, 2014, **41**, 050901.

24 I. E. Hill, M. Boyd, K. Milligan, C. A. Jenkins, A. Sorensen, A. Jirasek, D. Graham and K. Faulds, *Analyst*, 2023, **148**, 2594–2608.

25 E. Lipiec, B. R. Wood, A. Kulik, W. M. Kwiatek and G. Dietler, *Anal. Chem.*, 2018, **90**, 7644–7650.

26 M. Roman, T. P. Wrobel, A. Panek, C. Paluszkiewicz and W. M. Kwiatek, *J. Biophotonics*, 2020, **13**, e202000252.

27 B. Kästner, M. Marschall, A. Hornemann, S. Metzner, P. Patoka, S. Cortes, G. Wübbeler, A. Hoehl, E. Rühl and C. Elster, *Meas. Sci. Technol.*, 2024, **35**, 015403.

28 V. Ricciardi, M. Portaccio, L. Manti and M. Lepore, *Appl. Sci.*, 2020, **10**, 2974.

29 B. Wanjiku, K. Yamamoto, A. Klossek, F. Schumacher, H. Pischon, L. Mundhenk, F. Rancan, M. M. Judd, M. Ahmed, C. Zoschke, B. Kleuser, E. Rühl and M. Schäfer-Korting, *Anal. Chem.*, 2019, **91**, 7208–7214.

30 B. Ibáñez, A. Melero, A. Montoro, N. San Onofre and J. M. Soriano, *Curr. Issues Mol. Biol.*, 2024, **46**, 12718–12732.

31 H. Abramczyk, A. Imiela, B. Brozek-Pluska and M. Kopec, *Nanomedicine*, 2019, **14**, 1873–1888.

32 G. W. Auner, S. K. Koya, C. H. Huang, B. Broadbent, M. Trexler, Z. Auner, A. Elias, K. C. Mehne and M. A. Brusatori, *Cancer Metastasis Rev.*, 2018, **37**, 691–717.

33 P. F. Yang, J. Li, T. Y. Zhang, Y. X. Ren, Q. N. Zhang, R. F. Liu, H. N. Li, J. R. Hua, W. A. Wang, J. F. Wang and H. Zhou, *Cell Death Differ.*, 2023, **30**, 2432–2445.

34 S. J. Van Nest, L. M. Nicholson, N. Pavey, M. N. Hindi, A. G. Brolo, A. Jirasek and J. J. Lum, *BMC Cancer*, 2019, **19**, 474.

35 A. Pielesz, D. Binias, W. Waksmanska and R. Bobinski, *Spectrochim. Acta, Part A*, 2023, **286**, 121926.

36 K. E. Baidoo, K. Yong and M. W. Brechbiel, *Clin. Cancer Res.*, 2013, **19**, 530–537.

37 J. Rix, O. Uckermann, K. Kirsche, G. Schackert, E. Koch, M. Kirsch and R. Galli, *J. R. Soc. Interface*, 2022, **19**, 20220209.

38 K. Hanna, E. Krzoska, A. M. Shaaban, D. Muirhead, R. Abu-Eid and V. Speirs, *Br. J. Cancer*, 2022, **126**, 1125–1139.

39 D. R. Grimes, *JAMA Oncol.*, 2022, **8**, 949–949.

40 H. X. Li, Y. J. Xu, W. Q. Shi, F. Y. Li, Q. S. Zeng and C. Yi, *Int. J. Biochem. Cell Biol.*, 2017, **84**, 109–118.

41 J. Czapla-Masztafiak, J. Szlachetko, C. J. Milne, E. Lipiec, J. Sá, T. J. Penfold, T. Huthwelker, C. Borca, R. Abela and W. M. Kwiatek, *Biophys. J.*, 2016, **110**, 1304–1311.

42 K. Sailer, S. Viaggi and M. Nusse, *Int. J. Radiat. Biol.*, 1996, **69**, 601–613.

43 S. Dong, X. Lyu, S. Yuan, S. Wang, W. Li, Z. Chen, H. Yu, f. Li and Q. Jiang, *Radiat. Med. Prot.*, 2020, **1**, 179–185.

44 C. Mothersill, C. Seymour, A. Cocchetto and D. Williams, *Health Phys.*, 2024, **126**, 296–308.

45 R. Smith, H. Sellou, C. Chapuis, S. Huet and G. Timinszky, *Nucleic Acids Res.*, 2018, **46**, 6087–6098.